# On the Brillouin Zones of Glide-Symmetric Structures

Martin Petek, *Member, IEEE*, Jorge Alberto Tobón Vásquez, *Member, IEEE*, Guido Valerio, *Senior Member, IEEE*, Francisco Mesa, *Fellow, IEEE*, Oscar Quevedo-Teruel, *Fellow, IEEE*, and Francesca Vipiana, *Senior Member, IEEE*

***Abstract*—In this work, we investigate the appropriate definitions of the Brillouin zones and unit cells for glide-symmetric (GS) structures. In addition to translational periodicity, such structures possess glide symmetry; that is, invariance after a translation and a mirroring. Starting from basic concepts, we show that defining GS structures only by their translational periodicity leads to dispersion diagrams that are less clear and practical, similar to the effect observed when unnecessarily large periods are employed. In particular, we observe that the anisotropy of the structure is incorrectly assessed when following the definitions commonly adopted in the existing literature. Therefore, we introduce a modeling technique utilizing the multimodal transfer matrix method (MMTMM). This method can incorporate glide periodicity effectively, leading to an efficient solution as it operates with a reduced computational domain. It also leads to the demonstration of the effects of misleading definitions on various commonly used geometric configurations in the literature. The framework described here is applicable to any GS structure and facilitates the comparison of different types of unit cells.**

***Index Terms*—Electromagnetic bandgap materials, numerical analysis, periodic structures.**

## I. Introduction

PERIODIC structures find many applications in antenna engineering, as they allow the construction of tailored materials with properties not found in nature, designed with a specific material property [1], [2] such as electromagnetic band gap (EBG) materials [3], [4], or materials having unusual dispersive properties [5]. Due to the invariance of these structures with respect to a translation operator, their electromagnetic characteristics can be determined by restricting the simulation's computational domain to a single unit cell with periodic boundary conditions (PBCs). This is achieved by applying boundary conditions in line with the Floquet–Bloch theorem, that is, an eigenvalue problem defined within a unit cell on the translator operator defining the structure [6]. The unit cell is a subregion of the structure from which we can construct the complete structure with a translation operation. The smallest unit cell for which this is true is referred to as a primitive unit cell, while the larger unit cells are named supercells [7], [8]. Henceforth, we shall refer to this property as translational periodicity.

In recent years, the inclusion of glide symmetry in periodic antenna and microwave designs has been revisited [9]. glide symmetric (GS) structures are characterized by invariance with respect to a glide operator, i.e., the composition of a translation by half a period and a mirroring [10], [11], [12]. They can be implemented in 1-D or 2-D lattices. In the case of 2D-periodic structures, there exist two choices of introducing glide symmetry: either along only one of the lattice vectors, resulting in a 2D-periodic structure glide symmetric along one direction ($GS^{(1)}$), or along the two lattice vectors, resulting in a 2D-periodic structure glide symmetric along two directions ($GS^{(2)}$) [13]. More recently, hexagonal glide symmetric ($GS^{(hex)}$) structures have been studied [14]. Depending on the application, some of these configurations may improve the electromagnetic performance of antennas and other high-frequency components compared to conventional structures [15]. Consequently, numerous designs, using various types of unit cells, have been proposed, either exploiting their properties as EBG materials [16], or to use them instead of dielectric materials to implement a refractive index [9].

The significant interest raised by the introduction of glide symmetry has also led to the development of custom-fit specialized modeling techniques for their unique geometrical characteristics [17], [18], [19], [20], [21]. These techniques are based on a generalized Floquet theorem [10], [11], i.e., an eigenvalue problem defined within *half a unit cell* on the *glide operator* defining the structure. This theorem establishes how the electric field at a specific point is related to its GS

Received 16 April 2025; revised 14 October 2025; accepted 18 November 2025. Date of publication 11 December 2025; date of current version 13 February 2026. This work was supported in part by COST Action SyMat under Grant CA18223; in part by the Horizon Europe Research and Innovation Program through the GENIUS Project under Grant GA 101072560; in part by the Interreg Central Europe through the Project "MedWaveImage–Microwave Imaging Technology Transfer To Innovate the Medical Sector," under Grant CE0200670; in part by the Unite!–University Network for Innovation, Technology and Engineering. The work of Francisco Mesa was supported in part by MCIN/AEI/10.13039/501100011033 under Grant PID2020-116739GB-I00; and in part by C. J. Reddy Travel Grant for Graduate Students. *(Corresponding author: Francesca Vipiana.)*

Martin Petek, Jorge Alberto Tobón Vásquez, and Francesca Vipiana are with the Department of Electronics and Telecommunications, Politecnico di Torino, 10129 Turin, Italy (e-mail: martin.petek@polito.it; jorge.tobon@polito.it; francesca.vipiana@polito.it).

Guido Valerio is with the Laboratoire de Génie Électrique et Électronique de Paris (GeePs), Sorbonne Université, 75252 Paris, France, and also with GeePs, Université Paris-Saclay, 91192 Gif-sur-Yvette, France (e-mail: guido.valerio@sorbonne-universite.fr).

Francisco Mesa is with the Department of Applied Physics 1, ETS Ingeniería Informática, Universidad de Sevilla, 41012 Seville, Spain (e-mail: mesa@us.es).

Oscar Quevedo-Teruel is with the Division for Electromagnetic Engineering and Fusion Science, KTH Royal Institute of Technology, 100 Stockholm, Sweden (e-mail: oscarqt@kth.se).

This article has supplementary downloadable material available at https://doi.org/10.1109/TAP.2025.3640356, provided by the authors.

Digital Object Identifier 10.1109/TAP.2025.3640356

equivalent. The application of this theorem to GS structures is often presented as containing two branches, describing whether the mirroring part of the glide operation is performed over a perfect electric conductor (PEC) or perfect magnetic conductor (PMC) planes [17], [18]. In past work, both were used to obtain the complete solution. Sometimes, these branches are also referred to as parities [18]. These approaches facilitate the efficient derivation of eigenmode solutions, characterized by modal wavenumbers (describing propagation within the structure) and their frequency dependence. Typically, they are computed along the boundary of the irreducible Brillouin zone (IBZ), which is the smallest area encompassing unique solutions for a particular structure [6]. The plot of frequency versus the value of the wavenumber along the IBZ results in the dispersion diagram.

A characterizing feature of a GS structure is its particular modal configuration [15]. The study carried out in [18], [21], and [22] identified that these modes can be grouped in pairs characterized by opposite parities. However, inconsistencies are present in certain previously published dispersion diagrams, especially in the case of glide symmetry within the hexagonal lattice, as explored in our earlier research [22]. Using the standard definition of the IBZ, we derived a dispersion diagram that shows an apparent symmetry among solutions. However, given the IBZ definition, all solutions should be distinct [6]. In a square lattice, this symmetry is not apparent, yet the two parties share identical modal solutions in certain sections of the dispersion diagram [15]. Consequently, a natural question is whether they can be regarded as the same solution. A further issue is the comparison between glide and nonglide geometries. In some previous works, such comparisons were made using a supercell of the nonglide structure [15], [18]. The dispersion diagram that results has practical implications for lens design because establishing the equivalent refractive index involves an ad hoc judgment. This judgment depends on whether the second mode of the GS structure is considered a continuation of the first in certain parts of the dispersion diagram, but not in others [23], [24]. In [24], this choice is justified by observation of the field patterns. This work focuses on addressing these concerns; that is, is there a theoretical framework that can unify the approaches and tools applied to GS structures with those used for other periodic structures?

The novelty of this work lies in our analytical demonstration that, in GS structures, the two appearing branches exhibit identical frequency–wavevector behavior when the wavevector is shifted by a specific value. Furthermore, we propose a new approach to define the IBZ of GS structures. The new definition yields a more complete understanding of the electromagnetic characteristics of GS structures, particularly their anisotropy. We use the multimodal transfer matrix method (MMTMM) to set up the glide PBCs according to the generalized Floquet theorem, as previously done in [18]. However, we provide a more efficient solution of the eigenproblem than [18] by integrating the unit cell reduction approach with the linearization procedures reported in [22] and [25]. Additionally, the modeling approach introduced here can also handle structures $GS^{(1)}$ and $GS^{(hex)}$, which were not addressed in [18].

The results of this article shed new light on the dispersion diagrams of GS structures and their possible use. The proof that there exists a relationship between the two (+) and (−) branches of the dispersion diagram implies that it suffices to obtain one branch with the eigensolver, whereas the other can be subsequently derived. This fact, together with the unit cell reduction method, means less computational work is necessary to obtain dispersion diagrams of GS structures. The new definitions of the Brillouin zone provide a better framework to assess anisotropic effects and enable a better comparison with nonglide geometries. As dispersion diagrams are used as an initial step in designing periodic structures, this facilitates the design of components where they are used, for example, in lenses [23], [24], and EBG materials [26].

This article is organized as follows. In Section II, we present the theoretical fundamentals and describe the effects of analyzing the GS structures with the usual PBCs. In Section III, we describe numerical modeling with the MMTMM, which enables us to define the glide PBCs. Then, in Section IV, results using the method are presented and compared to the theoretical predictions. Further insights, comments, and consequences of this work are given in Section V. The conclusion is given in Section VI.

## II. Theoretical Consideration

This section provides a concise overview of the generalized Floquet theorem [10], [11], [17], which is subsequently further developed to explain the properties of the two modal branches typically observed in GS structures. Ultimately, we find that one branch is equivalent to the other when the wavevector is shifted by a specific amount. The discussion is centered on the electric field, although equivalent relations hold for the magnetic field. A time-harmonic dependence $e^{j\omega t}$ is assumed and suppressed throughout.

### A. 1-D Glide Symmetry

Consider a 1D-periodic structure (characterized by a 1-D lattice) that is glide periodic along the $x$-axis. For such a structure, the Floquet theorem states that the electric field $\mathbf{E}$ for any point in the structure is related to the electric field at the point after a translation by the period $p_x$ as

$$\mathbf{E}(x + p_x, y, z) = e^{-jk_x p_x}\mathbf{E}(x, y, z) \tag{1}$$

where $k_x$ is the Floquet wavenumber. A periodic structure can be defined by different choices of the period, but choosing the minimal period is optimal, as choosing a larger period than minimal results in the appearance of extra modes [27]. This effect is analogous to aliasing in sampling of signals [28].

If glide symmetry is present, the theorem can be further generalized following derivations in [10] and [11]. First, we define the "glide period" as

$$p_{gx} = p_x/2. \tag{2}$$

The generalized Floquet theorem is then

$$\mathbf{E}\left(x + p_{gx}, y, -z\right) = \pm e^{-jk_x p_{gx}}\mathbf{E}(x, y, z) \tag{3}$$

which provides a relation between a point in the structure and the point after a translation by glide period and a mirror image. Next, we note that

$$-\mathrm{e}^{-\mathrm{j}k_x p_{gx}} = \mathrm{e}^{-\mathrm{j}\pi}\mathrm{e}^{-\mathrm{j}k_x p_{gx}} = \mathrm{e}^{-\mathrm{j}(k_x+\pi/p_{gx})p_{gx}}. \tag{4}$$

Therefore, the $(-)$ branch provides the same solution as the $(+)$ branch, but at a shifted value of the wavevector

$$k_s = \frac{\pi}{p_{gx}} = \frac{2\pi}{p}. \tag{5}$$

In other words, the dispersion relation of the $(+)$ branch, $\omega_+$, and the $(-)$ branch, $\omega_-$, are related by

$$\omega_+(k_x) = \omega_-(k_x + k_s). \tag{6}$$

In the case of a structure GS$^{(1)}$, this relation holds along the glide-periodic dimension.

### B. 2-D Glide Symmetry

In a 2D-periodic structure (characterized by a 2-D lattice), the translational periodicity can be described with the lattice vectors $\mathbf{s}_1$ and $\mathbf{s}_2$ [7]. The Floquet theorem applies to each lattice vector and their sum and difference [18], that is

$$\mathbf{E}(\boldsymbol{\rho} + a\mathbf{s}_1 + b\mathbf{s}_2, z) = \mathrm{e}^{-\mathrm{j}\mathbf{k}_t\cdot(a\mathbf{s}_1+b\mathbf{s}_2)}\mathbf{E}(\boldsymbol{\rho}, z) \tag{7}$$

where $a, b = 0, \pm 1$, $\boldsymbol{\rho} = x\hat{\mathbf{x}} + y\hat{\mathbf{y}}$ is the position vector in the $xy$-plane and $\mathbf{k}_t = k_x\hat{\mathbf{x}} + k_y\hat{\mathbf{y}}$ is the transverse Floquet wavevector. The generalized Floquet theorem can be derived in a manner similar to that for 1-D glide-periodic structures. To do so, we first introduce the concept of glide-periodic lattice vectors, analogous to periodic lattice vectors [7]. As in the 1-D case, the "glide-periodic lattice vectors" describe the translation part of the glide symmetry operation. In [18], they are implicitly defined as half of the sum and difference of the lattice vectors. Thus, a structure GS$^{(2)}$ is invariant after a mirroring in z and a translation by either

$$\mathbf{s}_{g1} = \frac{\mathbf{s}_2 + \mathbf{s}_1}{2} \qquad \mathbf{s}_{g2} = \frac{\mathbf{s}_2 - \mathbf{s}_1}{2} \tag{8}$$

which leads to the generalized Floquet theorem in 2-D

$$\mathbf{E}(\boldsymbol{\rho} + \mathbf{s}_{g\xi}, -z) = g_\xi \mathbf{E}(\boldsymbol{\rho}, z) \tag{9}$$

with $\xi = 1, 2$. After a double glide symmetry operation, the electric field is related by the glide eigenvalues $g_\xi$ as

$$\mathbf{E}(\boldsymbol{\rho} + 2\mathbf{s}_{g\xi}, -(-z)) = g_\xi^2 \mathbf{E}(\boldsymbol{\rho}, z) \tag{10}$$

which again yields

$$g_\xi^2 = \mathrm{e}^{-\mathrm{j}\mathbf{k}_t\cdot(\mathbf{s}_2-(-1)^\xi\mathbf{s}_1)} \Rightarrow g_\xi = \pm\mathrm{e}^{-\mathrm{j}\mathbf{k}_t\cdot\mathbf{s}_{g\xi}}. \tag{11}$$

Here, $(-1)^\xi$ is introduced to switch between the sum or difference in (8). For either value of $\xi$, the same branch $(\pm)$ must be taken [18]. If we express the glide-periodic lattice vectors as $\mathbf{s}_{g\xi} = s_{g\xi}\hat{\mathbf{s}}_{g\xi}$, where $s_{g\xi} = |\mathbf{s}_{g\xi}|$, and define

$$k_{t,\xi} = \mathbf{k}_t \cdot \hat{\mathbf{s}}_{g\xi} \tag{12}$$

we can write the generalized Floquet theorem as

$$\mathbf{E}(\boldsymbol{\rho} + \mathbf{s}_{g\xi}, -z) = \pm\mathrm{e}^{-\mathrm{j}k_{t,\xi}s_{g\xi}}\mathbf{E}(\boldsymbol{\rho}, z) \qquad \xi = 1, 2. \tag{13}$$

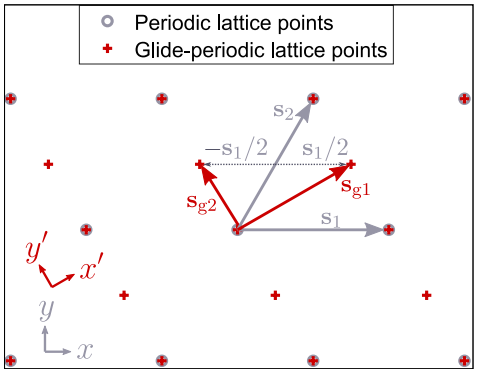


(a)

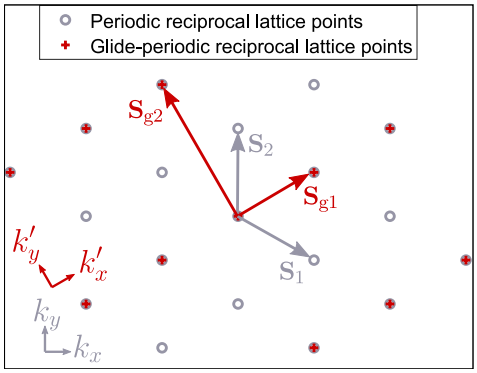


(b)

Fig. 1. 2-D lattice with nonorthogonal lattice vectors. (a) Direct space. (b) Reciprocal space.

As before, for each $\xi$ index, we can demonstrate that the branch $(-)$ is a shifted branch $(+)$; that is,

$$-\mathrm{e}^{-\mathrm{j}k_{t\xi}s_{g\xi}} = \mathrm{e}^{-\mathrm{j}(k_{t,\xi}+\pi/s_{g\xi})s_{g\xi}}. \tag{14}$$

This shift occurs twice, for each $\xi$. Thus, for pairs of the $(-)$ and the $(+)$ branches, the following relation holds:

$$\omega_-(\mathbf{k}_t) = \omega_+(\mathbf{k}_t + \mathbf{k}_{ts}) \tag{15}$$

where $\mathbf{k}_{ts}$ is the shift of the wavevector, given as a solution of the linear system of equations obtained from (14)

$$\mathbf{k}_{ts} = \pi\frac{\mathbf{s}_{g2}\times\hat{\mathbf{z}}}{\hat{\mathbf{z}}\cdot(\mathbf{s}_{g1}\times\mathbf{s}_{g2})} + \pi\frac{\hat{\mathbf{z}}\times\mathbf{s}_{g1}}{\hat{\mathbf{z}}\cdot(\mathbf{s}_{g1}\times\mathbf{s}_{g2})}. \tag{16}$$

### C. Construction of Unit Cells and Brillouin z Ones

Taking into account the earlier considerations, we now discuss the significance of defining and constructing the first Brillouin zone for periodic and for GS structures. Initially, a point and its periodic equivalents $(\circ)$ are expressed in direct space through the lattice vectors. In Fig. 1(a), the set of all these points forms a periodic lattice. Subsequently, the glide-periodic lattice vectors are defined in accordance with (8). Again in Fig. 1(a), the GS lattice points $(+)$ are obtained with a translation of the central point by an integer combination of or glide-periodic lattice vectors (8), thus forming a GS lattice.

Taking into account that the reciprocal lattice vectors are obtained as [6]

$$\mathbf{S}_1 = 2\pi\frac{\mathbf{s}_2\times\hat{\mathbf{z}}}{\hat{\mathbf{z}}\cdot(\mathbf{s}_1\times\mathbf{s}_2)} \qquad \mathbf{S}_2 = 2\pi\frac{\hat{\mathbf{z}}\times\mathbf{s}_1}{\hat{\mathbf{z}}\cdot(\mathbf{s}_1\times\mathbf{s}_2)} \tag{17}$$

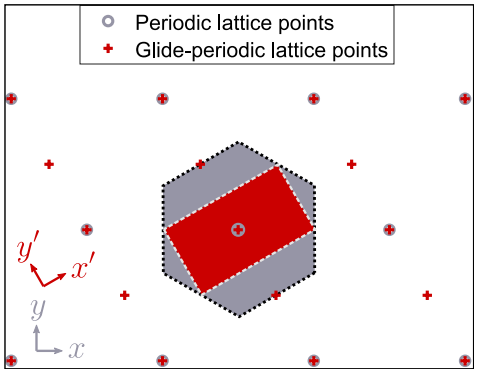


(a)

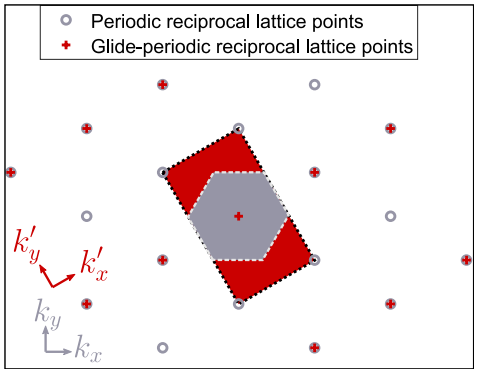


(b)

Fig. 2. Constructed (a) unit cells in the direct space, and (b) first Brillouin zone in the reciprocal space. The light-gray area is constructed from periodic lattice vectors, while the dark-red area is constructed from glide-periodic lattice vectors.

the key step in obtaining the appropriate Brillouin zone for GS structures is to replace the lattice vectors in (17) with those describing the smallest translations defining the structure. For the case of GS$^{(1)}$ structures with glide symmetry along $\mathbf{s}_1$, we replace this vector with the glide period $\mathbf{s}_g = \mathbf{s}_1/2$ to obtain

$$\mathbf{S}_g = 2\mathbf{S}_1 = 2\pi \frac{\mathbf{s}_2 \times \hat{\mathbf{z}}}{\hat{\mathbf{z}} \cdot (\mathbf{s}_g \times \mathbf{s}_2)} \qquad \mathbf{S}_2 = 2\pi \frac{\hat{\mathbf{z}} \times \mathbf{s}_g}{\hat{\mathbf{z}} \cdot (\mathbf{s}_g \times \mathbf{s}_2)}. \tag{18}$$

For GS$^{(2)}$ with lattice vectors given by (8), we have

$$\mathbf{S}_{g1} = 2\pi \frac{\mathbf{s}_{g2} \times \hat{\mathbf{z}}}{\hat{\mathbf{z}} \cdot (\mathbf{s}_{g1} \times \mathbf{s}_{g2})} \qquad \mathbf{S}_{g2} = 2\pi \frac{\hat{\mathbf{z}} \times \mathbf{s}_{g1}}{\hat{\mathbf{z}} \cdot (\mathbf{s}_{g1} \times \mathbf{s}_{g2})}. \tag{19}$$

The reciprocal lattice and its associated vectors are presented in Fig. 1(b), with the ($\circ$)-markers associated with periodic reciprocal lattice points, obtained after a translation of the central point with an integer sum of (17). The ($+$)-markers are equivalently obtained with the glide-periodic reciprocal lattice vectors (19). The regions of both the primitive unit cell and the first Brillouin zone can now be constructed by plotting bisectors of the lines connecting the central point [$(x, y) = (0, 0)$ for the direct lattice or $(k_x, k_y) = (0, 0)$ for the reciprocal lattice] to its adjacent points. This is done in Fig. 2(a) for the direct lattice. This figure shows an example with nonorthogonal lattice vectors where the primitive cell constructed by considering only the periodic lattice points is found to be a hexagon; this is the usual unit cell, which can be used to build the entire structure by multiple translation operations. The study of the periodic structure can be restricted to this single cell by imposing PBCs on its boundaries. By incorporating the GS periodicity, a different cell can be defined by means of the glide periods, whose area is reduced to the rectangular red region. This cell can be used to build the entire structure by multiple glide operations. The study of the periodic structure can be restricted to this single cell by enforcing glide PBCs on its boundaries. It is therefore clear that the glide-periodic structure is completely defined by a subdomain of its (gray) unit cell, which is called here the GS unit cell (in red in the figure).

The first Brillouin zones associated with these two regions are presented in Fig. 2(b). Note the inverse relationship between the physical size of the cell and the span of its associated first Brillouin zone, as a consequence of (19). In Fig. 2, we introduce a rotated (primed) coordinate system, as it is more natural to the GS unit cell.

The first Brillouin zone can often be further reduced to the IBZ. At this stage, the symmetries of the periodic structure are examined, such as mirror and rotational symmetries, and then directly applied to the reciprocal space. Furthermore, for any reciprocal (linear and time-invariant) structure, the solutions of $+\mathbf{k}_t$ are equal to $-\mathbf{k}_t$. Further details on the construction of Brillouin zones and determining the IBZ can be found in [29] and [6].

## III. Numerical Modeling

In this section, we use the generalized Floquet theorem to set the appropriate glide PBCs in the MMTMM. The MMTMM is a hybrid method with two steps. First, we need to obtain the coupling matrices of the multimodal ports surrounding the primitive unit cell in the frequency range of interest. In the scenario of a 1-D lattice, there exist two ports, while in the situation of a 2-D lattice, there are four. The solver used in this step is usually the CST frequency domain solver (CST FDS) with hexahedral meshing, as it allows placing the open boundary condition with touching ports [8], [30]. In a second postprocessing step, the translational periodic (or, where possible, glide-periodic) boundary conditions are set up, and the associated eigenvalue problem is solved. The solutions are obtained as complex wavenumber values for a given frequency, each of them associated with a Bloch mode of the structure.

### A. 1-D Lattice

Using $N$ modes in the waveports of the primitive unit cell, the equation for a one-dimensional (1-D)-MMTMM problem for a GS structure is given by [8], [18]

$$[\mathbf{T}]\,[\mathbf{F}_x] = [\mathbf{Q}][\mathbf{C}]\lambda_x\,[\mathbf{F}_x] \tag{20}$$

where $[\mathbf{T}]$ is the $2N \times 2N$ (ABCD) transfer matrix obtained with $N$ modes, $[\mathbf{F}_x]$ is the (unknown) eigenvector

$$[\mathbf{F}_x] = \begin{bmatrix} \mathbf{V}_x \\ \mathbf{I}_x \end{bmatrix} \tag{21}$$

with $\mathbf{V}_x$ and $\mathbf{I}_x$ being $N \times 1$ arrays containing the equivalent voltages and currents in the input/output ports. The eigenvalue

$\lambda_x$ represents the phase factor relating the eigenvectors at the input and output ports and is given in terms of the phase shift $k_x p_{gx}$ as

$$\lambda_x = \mathrm{e}^{-\mathrm{j}k_x p_{gx}} \tag{22}$$

where $k_x = \beta_x - \mathrm{j}\alpha_x$ is the modal wavenumber, with $\beta$ and $\alpha$ being the phase and attenuation constants, respectively. Note that we use here $p_{gx}$ because this is the distance between the two ports in the MMTMM (the ports are defined at the GS boundaries, $p_{gx} = p_g$). The correction matrix $[\mathbf{C}]$ is a diagonal matrix, introduced in this work to correct for an eventual difference in phase or amplitude of the port modes at the boundaries of the unit cell. The port eigensolver of CST FDS typically assigns the same phase and amplitude to a specific mode in the input and output ports. However, we found instances where the solver generates the same mode at opposite ports with a phase shift of 180°. The structure of this matrix is

$$[\mathbf{C}] = \begin{bmatrix} [\mathbf{c}_x] & [\mathbf{0}] \\ [\mathbf{0}] & [\mathbf{c}_x] \end{bmatrix} \tag{23}$$

where the diagonal matrix $[\mathbf{c}_x] = \mathrm{diag}[c_{x,1}, \ldots, c_{x,N}]$ contains the elements selected to carry out the necessary adjustment for the respective port mode.

Another key difference from the standard approach [8] is the introduction of the parity matrix $[\mathbf{Q}]$ [18]. This is again a diagonal matrix

$$[\mathbf{Q}] = \pm \begin{bmatrix} [\mathbf{q}_x] & [\mathbf{0}] \\ [\mathbf{0}] & [\mathbf{q}_x] \end{bmatrix} \tag{24}$$

with entries of $[\mathbf{q}_x] = \mathrm{diag}[p_{x,1}, \ldots, p_{x,N}]$ set to + 1(−1) if the corresponding port mode is even(odd) along the direction z. This matrix accounts for the mirroring operation of the glide periodicity and includes the possibility of choosing the (±) branches of (3). A detailed discussion on how to obtain the matrices $[\mathbf{Q}]$ and $[\mathbf{C}]$ is given in Section IV-A.

The solution to (20) is straightforward since the following linear eigenvalue problem is obtained by left-multiplying with $([\mathbf{Q}][\mathbf{C}])^{-1}$:

$$([\mathbf{Q}][\mathbf{C}])^{-1} [\mathbf{T}] [\mathbf{F}_x] = \lambda_x [\mathbf{F}_x]. \tag{25}$$

The eigenvalue $\lambda_x$ can be determined using any standard linear eigenvalue problem solver. Subsequently, the wavenumber can be derived by rearranging (22) as

$$k_x = \ln(\lambda_x) / (-\mathrm{j}p_x). \tag{26}$$

### B. 2-D Lattice

For a 2-D lattice, we can set the eigenvalue problem for glide-periodic boundaries as

$$[\widetilde{\mathbf{T}}] \begin{bmatrix} \mathbf{F}_x \\ \mathbf{F}_y \end{bmatrix} = [\mathbf{Q}][\mathbf{C}] \begin{bmatrix} \lambda_x \mathbf{F}_x \\ \lambda_y \mathbf{F}_y \end{bmatrix} \tag{27}$$

where $[\widetilde{\mathbf{T}}]$ is the permuted transfer matrix defined in [25], and the correction diagonal matrix $[\mathbf{C}]$ is given by

$$[\mathbf{C}] = \begin{bmatrix} [\mathbf{c}_x] & & & \\ & [\mathbf{c}_x] & & \\ & & [\mathbf{c}_y] & \\ & & & [\mathbf{c}_y] \end{bmatrix} \tag{28}$$

with $[\mathbf{c}_x]$ defined in the same way as in (23), and $[\mathbf{c}_y]$ similarly but now regarding the port modes in the $y$-direction. The internal structure of the diagonal parity matrix $[\mathbf{Q}]$ depends on the type of glide symmetry. For a $\mathrm{GS}^{(1)}$ structure, where the glide symmetry is along $x$, it is defined as

$$[\mathbf{Q}_{1D}] = \begin{bmatrix} \pm[\mathbf{q}_x] & & & \\ & \pm[\mathbf{q}_x] & & \\ & & [\mathbf{I}] & \\ & & & [\mathbf{I}] \end{bmatrix} \tag{29}$$

where $[\mathbf{q}_x]$ is defined as in (24) and the PBC along $y$ is set with the identity matrix $[\mathbf{I}]$. For a $\mathrm{GS}^{(2)}$ structure, the diagonal parity matrix is given by

$$[\mathbf{Q}_{2D}] = \pm \begin{bmatrix} [\mathbf{q}_x] & & & \\ & [\mathbf{q}_x] & & \\ & & [\mathbf{q}_y] & \\ & & & [\mathbf{q}_y] \end{bmatrix} \tag{30}$$

with $[\mathbf{q}_y]$ similarly defined as $[\mathbf{q}_x]$ but now for the port modes in the $y$-direction. It should be noted that the two (±) branches appearing in (13) are now reflected in the signs ± associated with $[\mathbf{Q}]$.

The original eigenvalue problem (27) is better rewritten as the following nonstandard eigenvalue problem:

$$[\widetilde{\mathbf{T}}_g] \begin{bmatrix} \mathbf{F}_x \\ \mathbf{F}_y \end{bmatrix} = \begin{bmatrix} \lambda_x \mathbf{F}_x \\ \lambda_y \mathbf{F}_y \end{bmatrix} \tag{31}$$

where

$$[\widetilde{\mathbf{T}}_g] = ([\mathbf{Q}][\mathbf{C}])^{-1} [\widetilde{\mathbf{T}}_=] \begin{bmatrix} [\widetilde{\mathbf{T}}_{g,xx}] & [\widetilde{\mathbf{T}}_{g,xy}] \\ [\widetilde{\mathbf{T}}_{g,yx}] & [\widetilde{\mathbf{T}}_{g,yy}] \end{bmatrix}. \tag{32}$$

The efficient solution of this eigenvalue problem for different cases of interest is discussed in the appendix.

## IV. Numerical Results

We now provide the specifics of the implementation and the results of the MMTMM analysis applied to periodic structures composed of pins. The structures are fully metallic, and losses are neglected by replacing the metal with the PEC. Incorporating conductor and dielectric losses does not alter the methodology in Section III because these losses can be inherently included via the multimodal transfer matrix computed using the full-wave simulator. In addition to validating the numerical method itself, we demonstrate the effects of using PBCs instead of glide PBCs to solve the eigenproblem of the GS structure. We analyze four distinct cases: 1-D-periodic structures, two-dimensional (2-D)-periodic structures with $\mathrm{GS}^{(1)}$, $\mathrm{GS}^{(2)}$ and $\mathrm{GS}^{(\mathrm{hex})}$. For each case, we present the results of scanning the cell path usually employed in the literature, and the proposed primitive cell path, which accounts for the glide periodicity. Both the (+) and (−) branches are calculated and discussed. In practice, one may only compute one of the branches and then follow the tables in this work to obtain the behavior of the other one. Henceforth, we will refer to the unit cell with only periodic boundaries as a periodic unit cell, and the minimum computational domain, defined with all possible glide-periodic boundaries, as the GS unit cell.

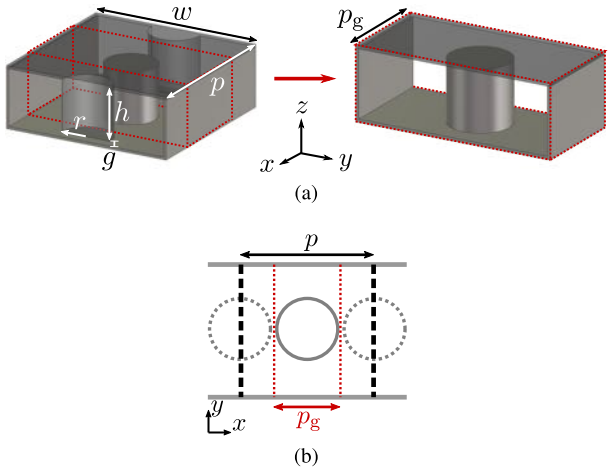


Fig. 3. Geometry of the GS structure in a 1-D lattice. (a) periodic unit cell (left) can be reduced to the GS unit cell (right). The dotted red lines mark the boundaries of the half-cell. (b) Top-down schematic of the structure, where the two dotted circles are pins at the top of the structure.

TABLE I
GEOMETRY PARAMETERS FOR STRUCTURES IN THIS WORK

| Variable | Meaning | Value [mm] |
|---|---|---|
| $p$ | translational period | 3.2 |
| $w$ | width of waveguide | 3.2 |
| $h$ | pin height | 1 |
| $g$ | gap between pin and floor/ceiling | 0.05 |
| $r$ | pin radius | 0.5 |
| $a$ | width of hexagon | 3.2 |

### A. 1-D Lattice

Consider the example of a rectangular waveguide with glide-periodic pins, as in the left of Fig. 3(a). The pins are alternately connected to the top and bottom metallic walls and are separated from the other wall by a small gap. The geometric parameters of the structure are given in Table I. In Fig. 3(a), the dotted red line marks the GS unit cell (depicted on the right), which is used with the MMTMM procedure. The top-down view of the lattice is presented in Fig. 3(b), where the glide period is

$$p_g = p/2. \tag{33}$$

To apply the MMTMM, first we must find the entries of the matrices [**C**] and [**Q**] in (25). The matrix [**C**] corrects the definition of the zero phase of two opposite ports, and its entries are determined by the algorithm employed to compute the port modes. Therefore, these entry values might vary for different solver settings, such as the mesh used. As an example, we examine the electric field configurations of the first, third, and fifth modes in Fig. 4(a), (c), and (e), respectively. These modes correspond to the same port and are arranged by frequency. Next, we compare these with the equivalent modes in Fig. 4(b), (d), and (f). We note that after a translation by $p_g\hat{\mathbf{x}}$, the first modes remain in phase. However, the third and fifth modes exhibit a 180° phase difference. Consequently, their contributions to the matrix [**C**] are 1, −1, and −1, respectively.

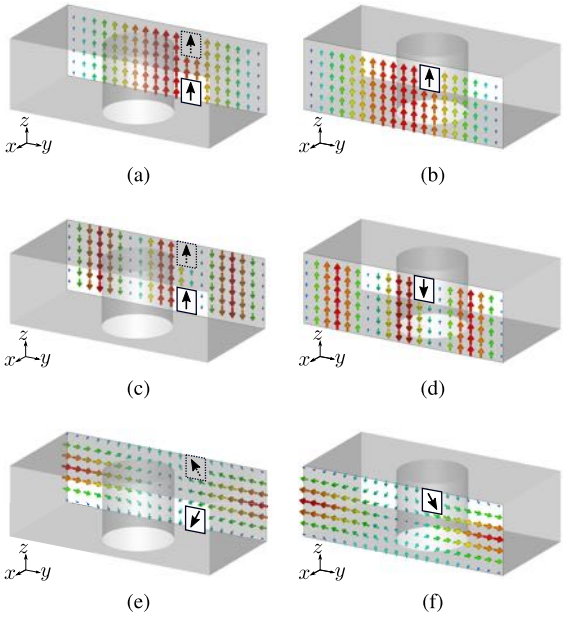


Fig. 4. Determining the entries of [**C**][**Q**] matrix. For each mode, we compare the z-component of the electric field at one port to its glide-periodic counterpart (in full line boxes). (a) Mode 1 at port 1. (b) Mode 1 at port 2. (c) Mode 3 of port 1. (d) Mode 3 of port 2. (e) Mode 5 of port 1. (f) Mode 5 of port 1.

We now determine the values of the parity matrix [**Q**]. We start by examining the z-component of the electric field for the first mode in Fig. 4(a). When we compare the orientation of the two arrows shown in the figure, we can see that this mode has even parity (z-components of the electric field are in-phase). The same observation can be made in Fig. 4(c) for the third mode. Similarly, the fifth mode can be determined to have odd parity in Fig. 4(e), as the vertical components are out-of-phase and the horizontal components are in-phase. Thus, the first, third, and fifth diagonal entries to [**Q**] would be 1, 1, −1. Note that, if the z-component is 0 for the entire field, the $y$-component may be used. If it is in-phase after mirroring (i.e. the mirroring plane is a PMC), the parity is −1, and if it is out-of-phase (i.e. the mirroring plane is a PEC), the parity is + 1.

The product of [**Q**] and [**C**] is better considered as a single matrix, and its values are obtained by comparing the electric field of the mode at one port to the electric field at the other port after a translation and a mirroring. Specifically, each entry is determined by checking if one mode transitions to the corresponding one in the opposite port via reflection across a PEC or PMC plane. However, separating them into two contributions may help to understand the effects of GS structures better. In establishing the glide PBCs (3) instead of the traditional PBCs (1), the distinction lies solely in the [**Q**] matrix, resulting from the mirroring operation. Therefore, given the same GS unit cell, if the most important port modes in MMTMM only have even parity, there is no discernible difference between solving the glide-periodic or periodic eigenproblem, and the electromagnetic performance of the associated structures will be similar [18].

The results of the MMTMM using $N = 13$ port modes for the structure in Fig. 3 are shown in Fig. 5. In the figure,

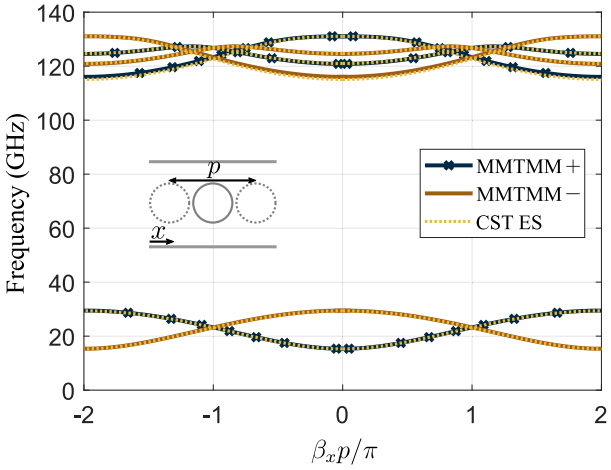


Fig. 5. Dispersion diagram for the GS structure in a 1-D lattice.

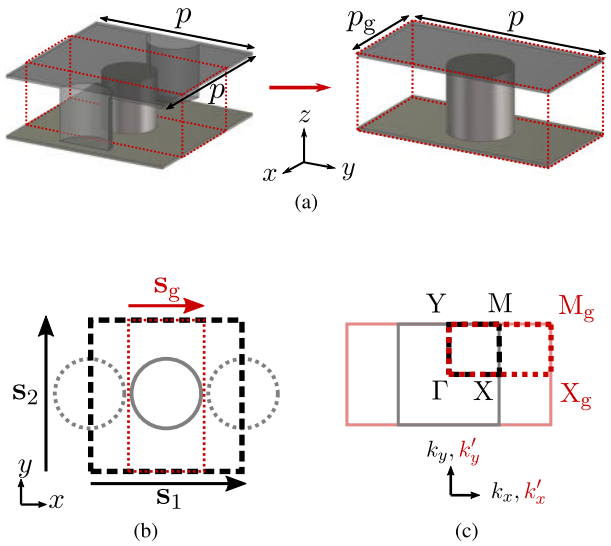


Fig. 6. Geometry of the GS$^{(1)}$ structure. (a) periodic unit cell (left) can be reduced to the GS unit cell (right). The dotted red lines mark the boundaries of the GS unit cell. (b) Top-down schematic of the structure. The full circles are bottom pins, and the dotted circles are top pins. (c) First Brillouin zone of the structure. The IBZ of the periodic unit cell is in a black dashed line. The IBZ of the GS unit cell is in a red dotted line.

an excellent agreement is observed between the proposed method and CST eigenvalue solver (CST ES), which uses the translation PBCs. Note that with the MMTMM, we directly obtain the full range of values of $\beta_x p/\pi$ from $-2$ to 2, and we can distinguish between the $(+)$ and $(-)$ branches in the dispersion diagram. As predicted by (4), the phase shift of the branch $(-)$ is that of the branch $(+)$, shifted by $2\pi$ (5).

### *B. 2-D Lattice, 1-D Glide Symmetry*

In this section, we examine a 2D-periodic structure that exhibits glide periodicity along the $x$-axis, referred to as GS$^{(1)}$. The unit cell of this structure is depicted in Fig. 6(a). The values of parameters are given in Table I with the only difference of the replacement of the PEC walls in Fig. 3 with PBCs at the $y$ edges of the unit cell in Fig. 6(a). The translational periodic lattice vectors are given by

$$\mathbf{s}_1 = p\hat{\mathbf{x}} \qquad \mathbf{s}_2 = p\hat{\mathbf{y}} \tag{34}$$

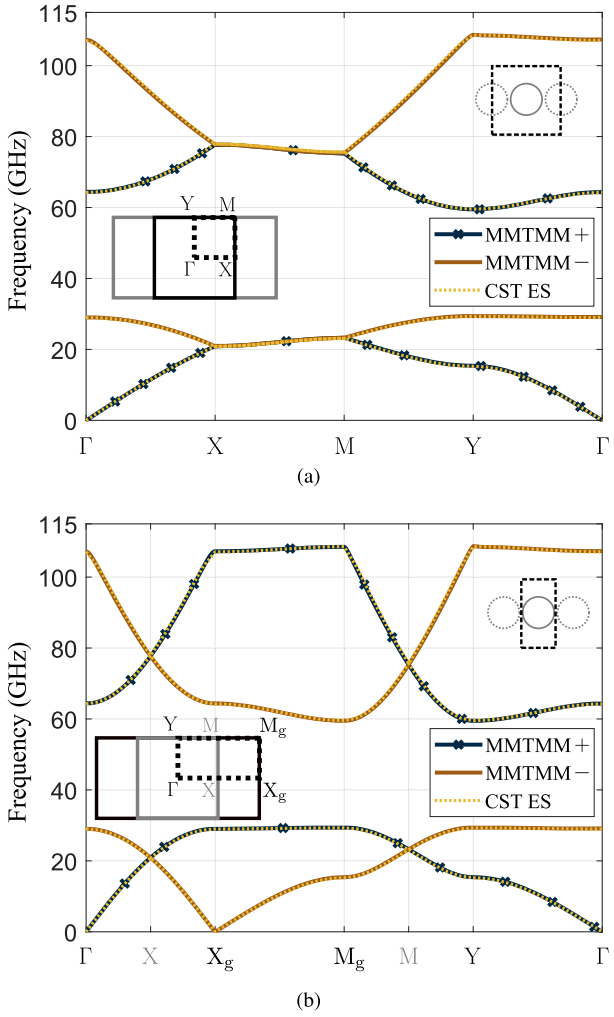


Fig. 7. Dispersion diagrams of the GS$^{(1)}$ structure: (a) neglecting the glide periodicity (commonly scanned path) and (b) accounting for the glide periodicity (proposed path).

and the glide-periodic lattice vector is ($p_g = p/2$)

$$\mathbf{s}_g = \mathbf{s}_1/2 = p_g\hat{\mathbf{x}}. \tag{35}$$

The top-down view of the structure is presented in Fig. 6(b). The first Brillouin zone of the periodic unit cell and the GS unit cell shown in Fig. 6(a) are depicted in Fig. 6(c). In this figure, the IBZ of the periodic unit cell and the GS unit cell are the dashed black and dotted red lines, respectively. The IBZ is here reduced to a quarter, since the structure possesses mirror symmetry over $xz$- and $yz$-planes, but not a 90° rotational symmetry about $\hat{\mathbf{z}}$.

The results of the MMTMM analysis are presented for two paths of the Brillouin zone. Fig. 7(a) shows the results concerning the path defined using only the period $p$ and Fig. 7(b) shows the results when the glide periodicity is also considered. The first six modes are retained in the MMTMM to resolve the eigenproblem. Since the paths are always along a constant value of $k_x$ or $k_y$, we use (43) or (44), according to the wavevector values $(k_x, k_y)$ for the critical points in the Brillouin zone in Table II. Here, we keep the same conventions as in [13], but we use the subscript g to distinguish between

TABLE II
WAVEVECTOR COMPONENTS AT CRITICAL POINTS OF THE IBZ OF THE STRUCTURE GS$^{(1)}$

| Point | $k_x$ | $k_y$ | $k'_x$ | $k'_y$ |
|---|---|---|---|---|
| $\Gamma$ | 0 | 0 | 0 | 0 |
| X | $\pi/p$ | 0 | $\pi/(2p_g)$ | 0 |
| $X_g$ | $2\pi/p$ | 0 | $\pi/p_g$ | 0 |
| $M_g$ | $2\pi/p$ | $\pi/p$ | $\pi/p_g$ | $\pi/p$ |
| M | $\pi/p$ | $\pi/p$ | $\pi/(2p_g)$ | $\pi/p$ |
| Y | 0 | $\pi/p$ | 0 | $\pi/p$ |

TABLE III
ACTUAL PATH OF (−) BRANCH AND EQUIVALENT PATH OF THE (+) BRANCH FOR GS$^{(1)}$ STRUCTURE

| Path of (−) | Equivalent path of (+) |
|---|---|
| $\overline{\Gamma X}$ | $\overline{X_g X}$ |
| $\overline{XM}$ | $\overline{XM}$ |
| $\overline{MY}$ | $\overline{MM_g}$ |
| $\overline{Y\Gamma}$ | $\overline{M_g X_g}$ |

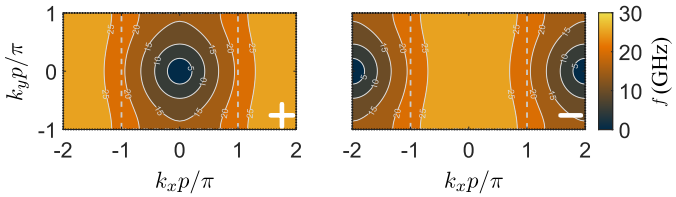


Fig. 8. Isofrequency maps for the first (+) and (−) branches for the GS$^{(1)}$ structure in Fig. 6. The $y$ axis is shared in the plots. The dashed lines delimit the first Brillouin zone of the periodic unit cell.

those obtained when considering the glide period $p_g$. We additionally introduce $k'_x$ and $k'_y$, which are the wavevector components in the coordinate system of the GS unit cell. In this GS unit cell, the orientation aligns with both $k_x$ and $k_y$, as the periodic and glide-periodic boundary orientations in Fig. 6(b) are identical.

As seen in Fig. 6(c), the main difference between the paths associated with the periodic unit cell and the GS unit cell is the removal of the section $\overline{XM}$ and the introduction of the section $\overline{XX_gM_gM}$. However, this additional path increases the amount of information in the dispersion diagram. Looking separately in Fig. 7(a) at the (+) and (−) branches in $\overline{\Gamma X}$, it can be observed that they do not reach the extreme value for this direction of propagation, as noted in Fig. 7(b) where we can observe that (+) branches continue to higher values after X. Thus, when reading the diagram in Fig. 7(a), we might incorrectly interpret that the stopband in the $\overline{XM}$ direction starts at about 20 GHz, when in fact $\overline{X_gM_g}$ is the proper boundary of the stopband in that direction, starting at about 30 GHz. Furthermore, the apparent anisotropies are different, as the $\overline{XM}$ and $\overline{X_gM_g}$ have different slopes. However, while the $\overline{XM}$ region does not provide any relevant information, the branch (−) in other sections of the IBZ in Fig. 7(a) is in fact shifted from the missing parts of the branch (+) in Fig. 7(b). The equivalent paths of the two branches are given in Table III.

The prediction by (6) that the solution at $k_x$ of the branch (−) is equivalent to that of the branch (+) shifted by $\pi/p_g$ is made more evident in the isofrequency maps shown in Fig. 8. The entire region presented in the figure is the first Brillouin zone of the GS unit cell. The dashed vertical lines delimit the region corresponding to the first Brillouin zone of the periodic unit cell, neglecting the glide periodicity.

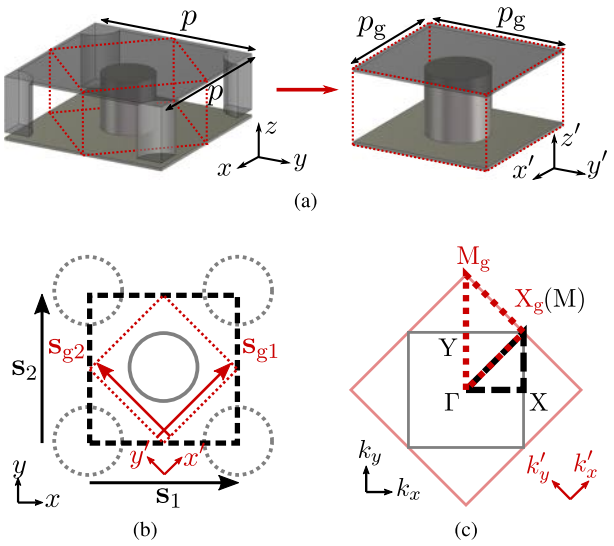


Fig. 9. Geometry of the GS$^{(2)}$ structure. (a) periodic unit cell (left) can be reduced to the GS unit cell (right). The dotted red lines mark the boundaries of the GS unit cell. (b) Top-down schematic of the structure. The full circles are bottom pins, and the dotted circles are top pins. (c) First Brillouin zone of the structure. The IBZ of the periodic unit cell is in a black dashed line. The IBZ of the GS unit cell is in a red dotted line.

### C. 2-D Lattice, 2-D Glide Symmetry

We proceed to examine the structure GS$^{(2)}$ shown in Fig. 9(a). Due to the identical periodicities along $x$ and $y$, the GS unit cell, along with its corresponding coordinate axes $x'$ and $y'$, is rotated by 45°, as illustrated in Fig. 9(b) [18]. The periodic lattice vectors are given by

$$\mathbf{s}_1 = p\hat{\mathbf{x}} \qquad \mathbf{s}_2 = p\hat{\mathbf{y}} \tag{36}$$

and the glide-periodic lattice vectors are ($p_g = p/\sqrt{2}$)

$$\mathbf{s}_{g1} = p_g\left(\frac{\hat{\mathbf{y}}+\hat{\mathbf{x}}}{\sqrt{2}}\right) \qquad \mathbf{s}_{g2} = p_g\left(\frac{\hat{\mathbf{y}}-\hat{\mathbf{x}}}{\sqrt{2}}\right). \tag{37}$$

As observed in Fig. 9, the structure is mirror-symmetric with respect to $xz$- and $yz$-planes. It also possesses symmetry with respect to a 90° rotation about $\hat{\mathbf{z}}$. Therefore, its IBZ is a triangular region, as depicted in Fig. 9(c). The paths $\overline{\Gamma YM\Gamma}$ and $\overline{\Gamma XM\Gamma}$ are equivalent due to the symmetries of the unit cell. As the GS unit cell is rotated compared to the periodic unit cell, this results in a rotation of its associated Brillouin zone. Furthermore, the corner point M in the first Brillouin zone of the periodic unit cell becomes equivalent to the side midpoint $X_g$ of the GS unit cell. Adhering to the convention that we scan the IBZ from $\Gamma$ to the midpoint of the unit cell and then the corner point, the path of the GS unit cell becomes $\overline{\Gamma X_g M_g \Gamma}$.

The results of the MMTMM analysis using the first six modes at each port are shown in Fig. 10, with the critical points defined in Table IV. Note that the path $\overline{\Gamma Y}$ contains

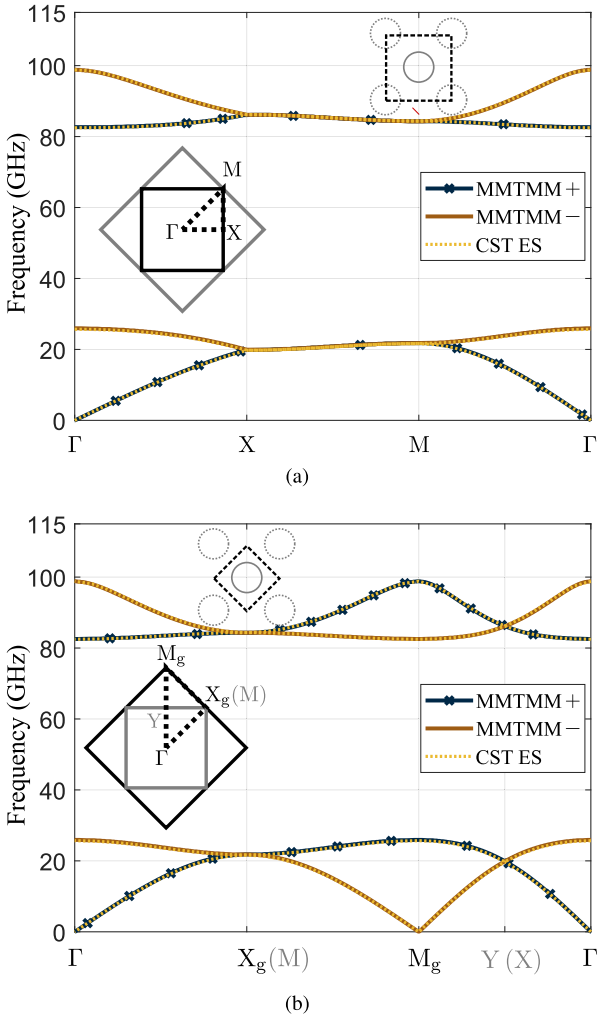


Fig. 10. Dispersion diagrams of the $GS^{(2)}$ structure: (a) neglecting the glide periodicity (commonly scanned path) and (b) accounting for the glide periodicity (proposed path).

TABLE IV
WAVEVECTOR COMPONENTS AT CRITICAL POINTS OF THE IBZ OF THE $GS^{(2)}$ STRUCTURE

| Point | $k_x$ | $k_y$ | $k'_x$ | $k'_y$ |
|---|---|---|---|---|
| Γ | 0 | 0 | 0 | 0 |
| X | $\pi/p$ | 0 | $\pi/(2p_g)$ | $-\pi/(2p_g)$ |
| Y | 0 | $\pi/p$ | $\pi/(2p_g)$ | $\pi/(2p_g)$ |
| $M_g$ | $2\pi/p$ | 0 | $\pi/p_g$ | $\pi/p_g$ |
| $X_g$ (M) | $\pi/p$ | $\pi/p$ | $\pi/p_g$ | 0 |

the same solutions to the path $\overline{\Gamma X}$ and the critical point X is equivalent to Y. For this unit cell, all paths except for $\overline{XM}$ and $\overline{M_g\Gamma}$ can again be resolved using either (43) or (44). The $\overline{XM}$ region, obtained with the primitive unit cell in the right of Fig. 10(a), requires the use of (47) with $n = -1$, while $\overline{M_g\Gamma}$ can be calculated using (42).

Scanning the IBZ of the GS unit cell $\overline{\Gamma X_g M_g \Gamma}$ replaces the section $\overline{XM}$ in Fig. 7(a) with $\overline{X_g M_g X}$ in Fig. 7(b). This results in a more correct interpretation of the properties of the dispersion diagram from the structure, as the $\overline{XM}$ appears at a lower frequency and has a smaller slope, resulting in an incorrect assessment of both stopband and propagative anisotropy. The equivalence paths of the branches are given in Table V.

TABLE V
ACTUAL PATH OF (−) BRANCH AND EQUIVALENT PATH OF THE (+) BRANCH FOR $GS^{(2)}$ STRUCTURE

| Path of (−) | Equivalent path of (+) |
|---|---|
| $\overline{\Gamma Y}$ ($\overline{\Gamma X}$) | $\overline{M_g Y}$ ($\overline{M_g X}$) |
| $\overline{XM}$ | $\overline{XM}$ |
| $\overline{M\Gamma}$ | $\overline{X_g M_g}$ |

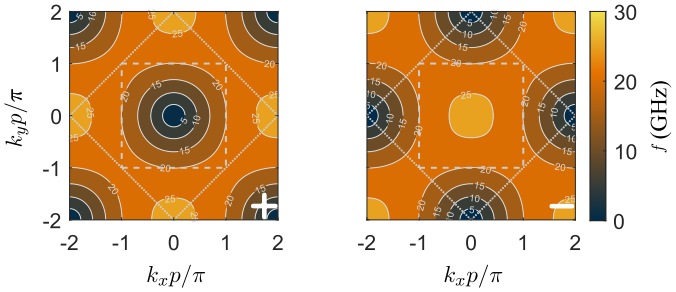


Fig. 11. Isofrequency maps for the first (+) and (−) branches for the $GS^{(2)}$ structure in Fig. 9. The $y$ axis is shared in the plots. The dashed and the dotted lines delimit the first Brillouin zone of the periodic unit cell and the GS unit cell, respectively.

The isofrequency maps for the first branch pairs can be observed in Fig. 11. In the figure, the dotted line presents the first Brillouin zone of the GS unit cell, while the dashed line represents the first Brillouin zone of the periodic unit cell. Considering the lattice vectors in (36), the predicted shift from (16) is $\mathbf{k}_{ts} = (2\pi/p)\hat{\mathbf{y}}$, as can be observed in Fig. 11.

### D. Hexagonal Lattice

The last, and most complex example, is the case of $GS^{(hex)}$ structure. Here, we will consider equilateral hexagons, which can alternatively be defined by a rhombic unit cell [31]. In this configuration, there are three equivalent choices of the rhombic geometry, resulting in a unit cell of the same size. Our choice is illustrated in Fig. 12(a), with its geometric parameters given in Table I. The sides of the rhomb are described by the following lattice vectors:

$$\mathbf{s}_1 = a\hat{\mathbf{x}} \qquad \mathbf{s}_2 = a\left[\sin(\pi/6)\,\hat{\mathbf{x}} + \cos(\pi/6)\,\hat{\mathbf{y}}\right]. \tag{38}$$

As these lattice vectors are not orthogonal, no effective difference is found between the structures obtained through either $GS^{(1)}$ or $GS^{(2)}$, as only one unique structure can be obtained [14]. Note that, after reducing the structure to the GS unit cell with glide-periodic boundaries, the GS unit cell on the right of Fig. 12(a) becomes rectangular, with the periodicities in the $x'y'$-coordinates given by

$$p_{gx'} = a\cos(\pi/6) \qquad p_{gy'} = a/2. \tag{39}$$

The glide-periodic lattice vectors in the $xy$-coordinate system are [see Fig. 12(b)]

$$\begin{aligned}\mathbf{s}_{g1} &= p_{gx'}\cos(\pi/6)\,\hat{\mathbf{x}} + p_{gx'}\sin(\pi/6)\,\hat{\mathbf{y}}\\ \mathbf{s}_{g2} &= -p_{gy'}\sin(\pi/6)\,\hat{\mathbf{x}} + p_{gy'}\cos(\pi/6)\,\hat{\mathbf{y}}.\end{aligned} \tag{40}$$

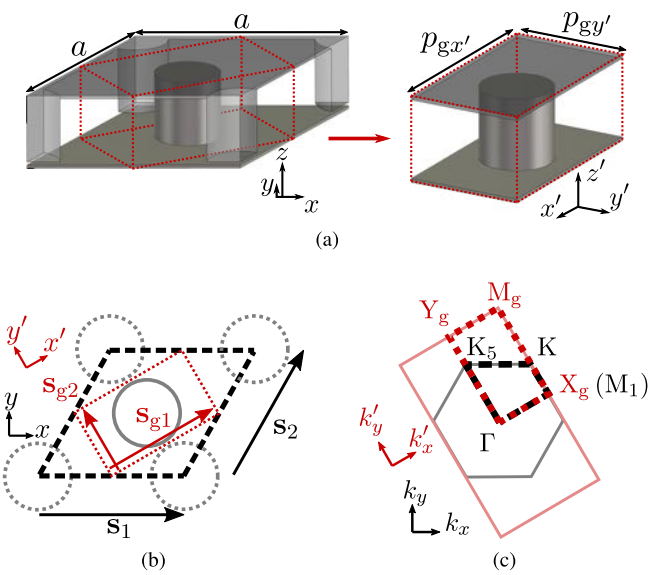


Fig. 12. Geometry of the GS$^{(hex)}$ structure: (a) periodic unit cell (left) can be reduced to the GS unit cell (right). The dotted red lines mark the boundaries of the GS unit cell. (b) Top-down schematic of the lattice. The full circles are bottom pins, and the dotted circles are top pins. (c) First Brillouin zone of the structure. The IBZ of the periodic unit cell is in a black dashed line. The IBZ of the GS unit cell is in a red dotted line.

TABLE VI

WAVEVECTOR COMPONENTS AT CRITICAL POINTS OF THE IBZ OF THE GS$^{(HEX)}$ STRUCTURE

| Point | $k_x$ | $k_y$ | $k'_x$ | $k'_y$ |
|---|---|---|---|---|
| Γ | 0 | 0 | 0 | 0 |
| $K_5$ | $-2\pi/(3a)$ | $\pi/\left(a\cos(\pi/6)\right)$ | 0 | $\frac{2}{3}\frac{\pi}{p_{gy'}}$ |
| $Y_g$ | $-\pi/a$ | $3\pi/\left(2a\cos(\pi/6)\right)$ | 0 | $\frac{\pi}{p_{gy'}}$ |
| K | $2\pi/(3a)$ | $\pi/\left(a\cos(\pi/6)\right)$ | $\pi/p_{gx'}$ | $\frac{1}{3}\frac{\pi}{p_{gy'}}$ |
| $M_g$ | 0 | $2\pi/\left(a\cos(\pi/6)\right)$ | $\pi/p_{gx'}$ | $\pi/p_{gy'}$ |
| $X_g$ ($M_1$) | $\pi/a$ | $\pi/\left(2a\cos(\pi/6)\right)$ | $\pi/p_{gx'}$ | 0 |

TABLE VII

ACTUAL PATH OF (−) BRANCH AND EQUIVALENT PATH OF THE (+) BRANCH FOR GS$^{(HEX)}$ STRUCTURE

| Path of (−) | Equivalent path of (+) |
|---|---|
| $\overline{\Gamma K_5}$ | $\overline{M_g K}$ |
| $\overline{K_5 K}$ | $\overline{K K_5}$ |
| $\overline{K M_1}$ | $\overline{K_5 Y_g}$ |
| $\overline{M_1 \Gamma}$ | $\overline{Y_g M_g}$ |

Similar to the structure GS$^{(2)}$, the two coordinate systems here are rotated, although here by 30°. This rotation also appears in the Brillouin zone, as illustrated in Fig. 12(c). It is important to mention that, although the translational periodic lattice vectors are nonorthogonal, the glide-periodic lattice vectors are orthogonal. Thus, the first Brillouin zone of the periodic unit cell is a hexagon, while the first Brillouin zone of the GS unit cell is the rectangular region.

The results of the MMTMM analysis using the first six modes in the input/output ports are presented in Fig. 13.

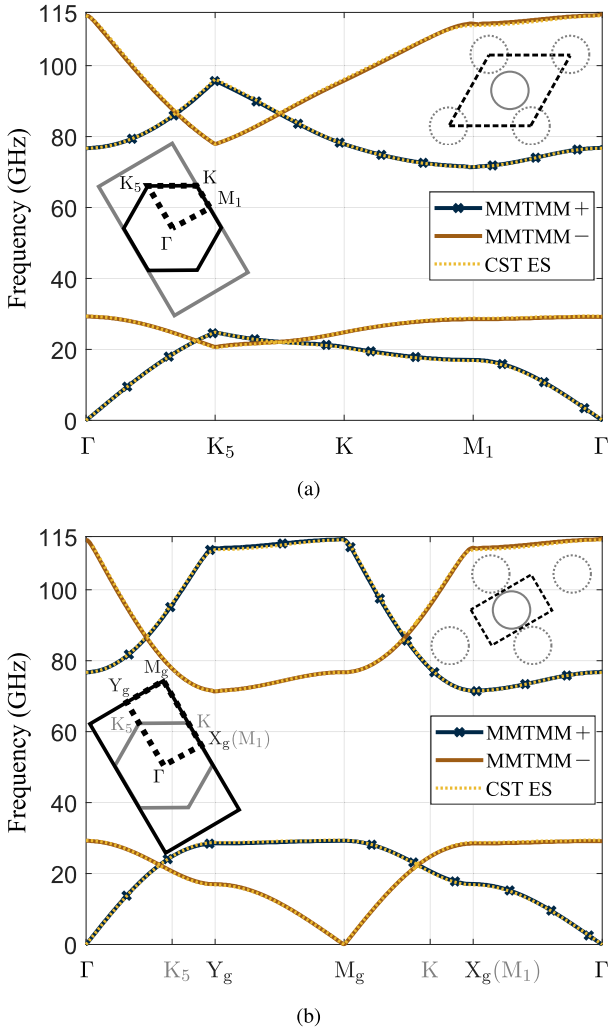


Fig. 13. Dispersion diagrams of the GS$^{(hex)}$ structure: (a) neglecting the glide periodicity (commonly scanned path) and (b) accounting for the glide periodicity (proposed path).

The wavevector components at critical points are given in Table VI. All sections, except for $\overline{K_5 K}$, are obtained using the linearized formulations (43) or (44). The section $\overline{K_5 K}$ requires the resolution of the polynomial eigenvalue problem (47), as in [22]. As previously noted, Fig. 13(a) illustrates some insufficiencies caused by the use of the previously identified IBZ [14], [22]. It is notable that the branches in $\overline{\Gamma K_5}$ intersect and terminate suddenly, displaying a clear symmetry around the midpoint of the $\overline{K_5 K}$ section. Furthermore, we note that unlike for $\overline{\Gamma X}$ in the case of GS$^{(2)}$, the (−) branch may not be used to extend the (+) branch in $\overline{\Gamma K_5}$, as evident in Fig. 13(b). The equivalence of different sections in the dispersion diagram is given in Table VII. Considering (40), the computed shift with (16) is

$$\mathbf{k}_{ts} = \frac{2\pi}{a\cos(\pi/6)}\hat{\mathbf{y}} \tag{41}$$

which is exactly the value observed in Fig. 14, where the isofrequency plots are presented for the first pair of each branch.

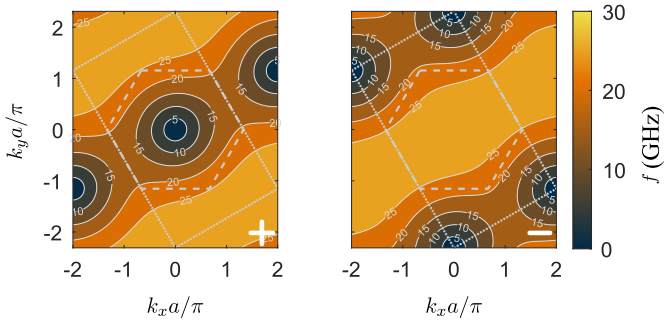


Fig. 14. Isofrequency maps for the first (+) and (−) branches for the GS$^{(\mathrm{hex})}$ structure in Fig. 12. The $y$ axis is shared in the plots. The dashed and the dotted lines delimit the first Brillouin zone of the periodic unit cell and the GS unit cell, respectively.

### *E. Full-Wave Validation*

Here, we further investigate whether the (−) branch is a physically meaningful solution, located at the *nonshifted* values of the wavevector. Taking into account that the (+) and (−) branches are simply related through the shift (16), it is worth to investigate whether the spectral components of the (−) branch are solutions present in the periodic structure, or they could be considered "extra modes", as in the case of supercells [27]. We explore this issue by deriving the spectral components, shown as isofrequency curves, using a method that does not inherently presuppose a particular periodicity.

The above study is carried out by exciting a finite periodic structure and examining the resulting spectral components via the Fourier transform of the electric field components, as detailed in [32]. Two structures are compared: the GS$^{(2)}$ from Fig. 9(a) and a conventional 2D-periodic pin structure with the period equal to the glide period in Table I (i.e., a structure where the top pins are instead placed on the bottom). Both structures have a dimension of $20p \times 20p$ and the E-field is excited by a z-aligned discrete port, located at a central pin. An investigation of the electric field at 10 GHz on the glide plane is conducted. The results can be found in Fig. 15, where the plots in the same column belong to the same structure (left for the nonglide and right for the glide case) and the rows depict the magnitude of the Fourier transform of the $x$, $y$, and z field components, respectively. The white circles are the isofrequency curves of the solution obtained by CST ES. The results in the second column for the case of glide symmetry demonstrate that the spectral solutions corresponding to the (−) branch (here plotted as dotted circular lines) are present both in the $E_x$ and $E_y$ components, while the $E_z$ only shows contributions associated with the (+) branch. This means that the solution of the (−) branch has physical meaning by itself and is not an alias of the solution in the (+) branch at the shifted value of the wavevector given by (16). Therefore, (15) must be interpreted as a relation of dispersion curves of two distinct physical solutions, both of which exist in the structure. This is consistent with the results in [32], where such an analysis was done for a 1-D glide-periodic structure.

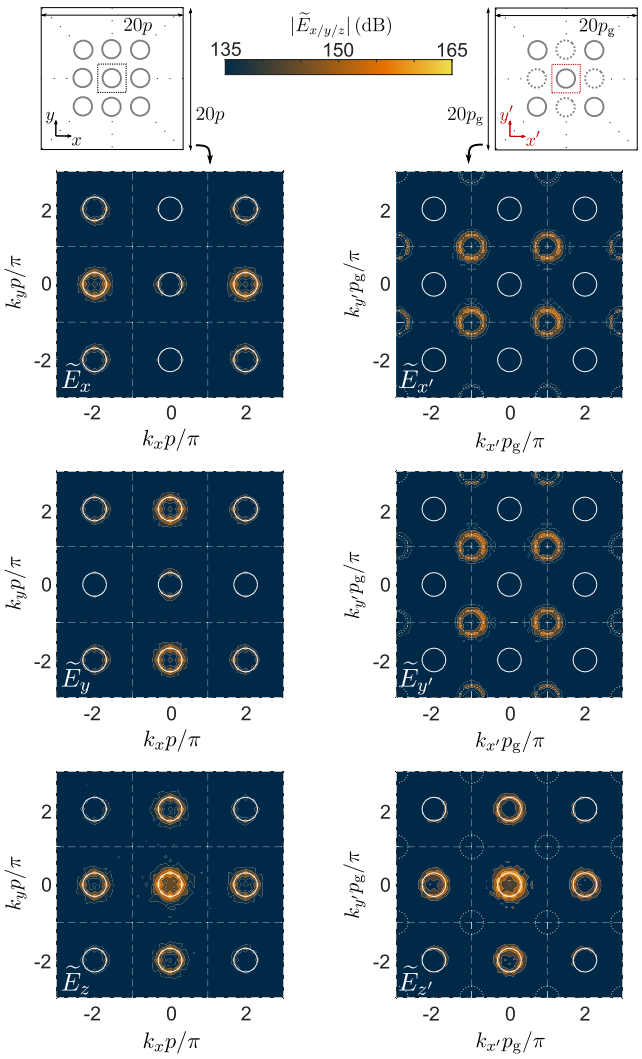


Fig. 15. Spectral components in a finite periodic structure, schematically depicted in the top. The first column corresponds to a regular pin structure (with $p = p_g$) and the second to a GS$^{(2)}$ with geometrical parameters in Table I. The rows show the magnitude of the Fourier transform of the $x$, $y$, and z field components, respectively.

## V. Discussion

In this section, we offer additional context regarding earlier research and its connection to the theory introduced in this article. Some additional considerations are included in the supplementary materials to this article. First, we would like to reiterate that the definitions of the IBZ should consider the glide periodicity, even if the eigenproblem is solved with PBCs. Unfortunately, in this case, the information on the branch of the solution in the dispersion diagram is lost. It would be reasonable to assume that the lowest frequency bound at Γ of a fundamental mode is provided by a (+) branch, but there appears to be no pattern with higher frequency modes. In the example with GS$^{(2)}$ pins in this article, the pattern is (+), (−), (+), (−), while for GS$^{(2)}$ holes it is (+), (−), (−), (+) [21]. Most probably, this order depends on both the kind of geometry and its specific parameters. Our recommendation is, therefore, whenever possible, to use a method that allows setting glide-periodic boundaries. If not feasible, we nevertheless recommend using the path that accounts for the glide periodicity when computing the dispersion diagram of the structure,

even if distinguishing between the branches is not possible in this way.

The dispersion diagram is often used to identify the stopband of the structure. Fortunately, the overall stopband, where the unit cell functions as an EBG in all possible directions, remains unchanged when the periodic unit cell or one of its supercells is used for simulation. However, following the previous conventions, the stopband anisotropy may be improperly read from the diagrams. Thus, when interpreting the previously published results of the stopband attenuation evaluation [20], [21], [22], [24], [30], it is important to consider the missing section of the proposed path (for example, $\overline{\mathrm{X_gM_g}}$ in Fig. 10). This missing section may be extracted by consulting the Tables III, V, and VII in Section IV. Furthermore, previous research reveals a notable observation regarding the stopband behavior of $\mathrm{GS}^{(2)}$ structures: at X, no stopband modes are present [21], [30]. Similar behavior was found for $\mathrm{GS}^{(\mathrm{hex})}$ structures, where there are no stopband modes in $\overline{\mathrm{KK_5}}$ [22]. The theory outlined here clarifies that these points are not genuinely the critical points; instead, they are the intermediate points within the first Brillouin zone.

Another use of the dispersion diagram is to extract the equivalent refractive index for different directions of propagation, which is used for lens antenna design. In a recent article, using a $\mathrm{GS}^{(2)}$ structure, the second mode is considered an extension of the first in $\overline{\Gamma\mathrm{X}}$, but only the first mode is used in the $\overline{\mathrm{M}\Gamma}$ section [24]. This choice is justified by looking at the field patterns. Presenting the graphs in the way as in Fig. 10(b) makes it more apparent that the (+) branch in $\overline{\Gamma\mathrm{X}}$ continues and reaches the maximum at $\mathrm{M_g}$, while the two branches in $\overline{\Gamma\mathrm{X_g}}$ may not be used as a continuation of one another.

An alternative technique that makes it possible to work with reduced unit cells is the method of moments employing a specialized Green's function [21]. Comparing the results presented here to [21], we can note that the (+) and (−) branches are switched. This is because of the different definitions of (+) and (−) parities: in [21], the branch (−) is defined to correspond to the one where the current is translated and subsequently mirrored over PEC, while the branch (+) is mirrored over the PMC. Therefore, this discrepancy is only in the nomenclature, as here we define the PEC-related branch to be (+).

Furthermore, we note that the effect of merging of the modes is also apparent in other kinds of higher symmetries, for example, twist symmetries [10], [33]. However, when translation is not involved in the higher symmetry, this behavior is not observed, as exemplified by the mirror half-turn symmetry studied in [14] and [21]. Therefore, we may conjecture that the results of this work may be extended to higher symmetries that involve a translational operator.

Finally, it should be noted that the theory discussed in this study is rigorous only under conditions of perfect glide symmetry. Deviations from glide symmetry will induce the formation of a stopband around the meeting point of the (+) and (−) branches [34]. In that case, standard definitions of the Brillouin zones apply.

## VI. Conclusion and Perspectives

In this work, we demonstrated that neglecting the glide periodicity results in a definition of the Brillouin zone analogous to that of a supercell. We provide a recipe for the construction of proper Brillouin zones for GS geometries and propose an efficient numerical method based on MMTMM to easily resolve the paths in IBZ. This method was used to demonstrate the effects of inappropriate definitions of the unit cell and Brillouin zone. As dispersion diagrams are frequently used to understand the properties of periodic structures, the results of this work facilitate the understanding and design of GS structures.

The concepts presented in this work are likely to be extendable to other kinds of higher symmetries, where a generalization of the Floquet theorem exists, for example, as with twist symmetries [10], [33].

## Acknowledgment

The authors thank Prof. Eva Rajo-Iglesias and Dr. Nelson Castro Salas for helpful insights and discussions regarding Section IV-E.

## Appendix

The eigenproblem (31) can be directly resolved for the case where $\lambda_x = \lambda_y$ as it defines a linear eigenvalue problem

$$[\widetilde{\mathbf{T}}_{\mathrm{g}}]\begin{bmatrix}\mathbf{F}_x\\ \mathbf{F}_y\end{bmatrix} = \lambda_x \begin{bmatrix}\mathbf{F}_x\\ \mathbf{F}_y\end{bmatrix}. \tag{42}$$

However, this only resolves the diagonal path $k_x p_x = k_y p_y$ in the Brillouin zone. For other paths, (31) defines a nonlinear eigenproblem since it contains two eigenvalues. For paths where one of the eigenvalues is constant (fixed), it can be linearized to [25]

$$\lambda_y \text{ fixed: } \left([\widetilde{\mathbf{T}}_{\mathrm{g},xx}] + [\widetilde{\mathbf{T}}_{\mathrm{g},xy}][\mathbf{R}_y][\widetilde{\mathbf{T}}_{\mathrm{g},yx}]\right)\mathbf{F}_x = \lambda_x \mathbf{F}_x \tag{43}$$

$$\lambda_x \text{ fixed: } \left([\widetilde{\mathbf{T}}_{\mathrm{g},yy}] + [\widetilde{\mathbf{T}}_{\mathrm{g},yx}][\mathbf{R}_x][\widetilde{\mathbf{T}}_{\mathrm{g},xy}]\right)\mathbf{F}_y = \lambda_y \mathbf{F}_y\,. \tag{44}$$

Above, $[\mathbf{R}_\nu]$ contains the value of the fixed wavenumber $k_\nu$ as

$$[\mathbf{R}_\nu] = \left(\lambda_\nu[\mathbf{I}] - [\widetilde{\mathbf{T}}_{\mathrm{g},\nu\nu}]\right)^{-1} \qquad \nu \equiv x, y. \tag{45}$$

For paths defined the following linear relationship between the phase shifts:

$$k_y p_y = s k_x p_x + k_{x0} p_x \tag{46}$$

we can use a different method. In (46), $k_{x0}p_x$ is the offset and $s$ the slope. In this case, we can express the problem as [22]

$$\left(\left[\mathbf{M}_{n+1,x}\right]\lambda_x^{n+1} + \left[\mathbf{M}_{n,x}\right]\lambda_x^{n} + \left[\mathbf{M}_{1,x}\right]\lambda_x + \left[\mathbf{M}_{0,x}\right]\right)\mathbf{F}_x = [\mathbf{0}] \tag{47}$$

with

$$\begin{aligned}\left[\mathbf{M}_{n+1,x}\right] &= \lambda_{y0}[\widetilde{\mathbf{T}}_{\mathrm{g},xy}]^{-1}\\ \left[\mathbf{M}_{n,x}\right] &= -\lambda_{y0}[\widetilde{\mathbf{T}}_{\mathrm{g},xy}]^{-1}[\widetilde{\mathbf{T}}_{\mathrm{g},xx}]\\ \left[\mathbf{M}_{1,x}\right] &= -[\widetilde{\mathbf{T}}_{\mathrm{g},yy}][\widetilde{\mathbf{T}}_{\mathrm{g},xy}]^{-1}\\ \left[\mathbf{M}_{0,x}\right] &= [\widetilde{\mathbf{T}}_{\mathrm{g},yy}][\widetilde{\mathbf{T}}_{\mathrm{g},xy}]^{-1}[\widetilde{\mathbf{T}}_{\mathrm{g},xx}] - [\widetilde{\mathbf{T}}_{\mathrm{g},yx}].\end{aligned} \tag{48}$$

The factor $\lambda_{y0} = \mathrm{e}^{-\mathrm{j}k_{x0}p_x}$ arises due to the offset in (46). If $s$ is an integer, (47) can be solved as a polynomial eigenvalue problem [22] making use of companion matrices [35]. If required, an equivalent relationship can be derived by substituting $x \to y$ and $y \to x$ into (46)–(48) [22].

## REFERENCES


[1] P. Kumar, T. Ali, and M. M. M. Pai, "Electromagnetic metamaterials: A new paradigm of antenna design," *IEEE Access*, vol. 9, pp. 18722–18751, 2021.

[2] C. Milias et al., "Metamaterial-inspired antennas: A review of the state of the art and future design challenges," *IEEE Access*, vol. 9, pp. 89846–89865, 2021.

[3] P. Samineni, T. Khan, and A. De, "Modeling of electromagnetic band gap structures: A review," *Int. J. RF Microw. Comput.-Aided Eng.*, vol. 27, no. 2, Feb. 2017, Art. no. e21055.

[4] I. Shahid, D. Thalakotuna, D. K. Karmokar, S. J. Mahon, and M. Heimlich, "Periodic structures for reconfigurable filter design: A comprehensive review," *IEEE Microw. Mag.*, vol. 22, no. 11, pp. 38–51, Nov. 2021.

[5] R. C. Rumpf, *Engineering the Dispersion and Anisotropy of Periodic Electromagnetic Structures*(Solid State Physics), vol. 66, R. E. Camley and R. L. Stamps, Eds., New York, NY, USA: Academic, 2015, ch. 3, pp. 213–300.

[6] J. D. Joannopoulos, S. G. Johnson, J. N. Winn, and R. D. Meade, *Molding the Flow of Light*, vol. 12. Princeton, NJ, USA: Princeton Univ. Press, 2008.

[7] N. W. Ashcroft and N. S. D. Mermin, *Solid State Physics*. New York, NY, USA: Holt.Saunders, 1976.

[8] F. Mesa, G. Valerio, R. Rodriguez-Berral, and O. Quevedo-Teruel, "Simulation-assisted efficient computation of the dispersion diagram of periodic structures: A comprehensive overview with applications to filters, leaky-wave antennas and metasurfaces," *IEEE Antennas Propag. Mag.*, vol. 63, no. 5, pp. 33–45, Oct. 2021.

[9] O. Quevedo-Teruel, M. Ebrahimpouri, and M. Ng Mou Kehn, "Ultrawideband metasurface lenses based on off-shifted opposite layers," *IEEE Antennas Wireless Propag. Lett.*, vol. 15, pp. 484–487, 2016.

[10] A. Hessel, M. Hui Chen, R. C. M. Li, and A. A. Oliner, "Propagation in periodically loaded waveguides with higher symmetries," *Proc. IEEE*, vol. 61, no. 2, pp. 183–195, Feb. 1973.

[11] P. J. Crepeau and P. R. McIsaac, "Consequences of symmetry in periodic structures," *Proc. IEEE*, vol. 52, no. 1, pp. 33–43, Jan. 1964.

[12] S. Amari, R. Vahldieck, and J. Bornemann, "Accurate analysis of periodic structures with an additional symmetry in the unit cell from classical matrix eigenvalues," *IEEE Trans. Microw. Theory Techn.*, vol. 46, no. 10, pp. 1513–1515, Oct. 1998.

[13] Z. Sipus, K. Cavar, M. Bosiljevac, and E. Rajo-Iglesias, "Glide-symmetric holey structures applied to waveguide technology: Design considerations," *Sensors*, vol. 20, no. 23, p. 6871, Dec. 2020.

[14] S. Yang, O. Zetterstrom, F. Mesa, and O. Quevedo-Teruel, "Dispersion analysis of metasurfaces with hexagonal lattices with higher symmetries," *IEEE J. Microw.*, vol. 3, no. 4, pp. 1154–1165, Oct. 2023.

[15] O. Quevedo-Teruel, Q. Chen, F. Mesa, N. J. G. Fonseca, and G. Valerio, "On the benefits of glide symmetries for microwave devices," *IEEE J. Microw.*, vol. 1, no. 1, pp. 457–469, Jan. 2021.

[16] L. F. Herrán, A. Algaba Brazalez, and E. Rajo-Iglesias, "Ka-band planar slotted waveguide array based on groove gap waveguide technology with a glide-symmetric holey metasurface," *Sci. Rep.*, vol. 11, no. 1, p. 8697, Apr. 2021.

[17] G. Valerio, F. Ghasemifard, Z. Sipus, and O. Quevedo-Teruel, "Glide-symmetric all-metal holey metasurfaces for low-dispersive artificial materials: Modeling and properties," *IEEE Trans. Microw. Theory Techn.*, vol. 66, no. 7, pp. 3210–3223, Jul. 2018.

[18] M. Bagheriasl, O. Quevedo-Teruel, and G. Valerio, "Bloch analysis of artificial lines and surfaces exhibiting glide symmetry," *IEEE Trans. Microw. Theory Techn.*, vol. 67, no. 7, pp. 2618–2628, Jul. 2019.

[19] B. Fischer and G. Valerio, "Quasi-static homogenization of glide-symmetric holey parallel-plate waveguides with ultra-wideband validity," *IEEE Trans. Antennas Propag.*, vol. 70, no. 11, pp. 10569–10582, Nov. 2022.

[20] D. Tomić and Z. Šipuš, "Rigorous coupled wave analysis of parallel-plate waveguides loaded with glide-symmetric dielectric structures," *IEEE Trans. Microw. Theory Techn.*, vol. 72, no. 8, pp. 4542–4554, Aug. 2024.

[21] M. Petek, J. Rivero, J. A. T. Vásquez, G. Valerio, O. Quevedo-Teruel, and F. Vipiana, "Method of moments for the dispersion modeling of glide-symmetric periodic structures," *IEEE Trans. Antennas Propag.*, vol. 72, no. 1, pp. 756–766, Jan. 2024.

[22] M. Petek et al., "Numerical modeling of higher-symmetric periodic structures with a hexagonal lattice," *IEEE Trans. Antennas Propag.*, vol. 73, no. 3, pp. 1650–1661, Mar. 2025.

[23] J.-M. Poyanco, O. Zetterstrom, P. Castillo-Tapia, N. J. G. Fonseca, F. Pizarro, and O. Quevedo-Teruel, "Two-dimensional glide-symmetric dielectric structures for planar graded-index lens antennas," *IEEE Antennas Wireless Propag. Lett.*, vol. 20, no. 11, pp. 2171–2175, Nov. 2021.

[24] D. Tomić, J.-M. Poyanco, E. Rajo-Iglesias, and Z. Šipuš, "Exploring the potential of a coaxial unit cell: Metalens antenna design based on a highly isotropic metallic periodic structure," *IEEE Trans. Antennas Propag.*, vol. 72, no. 11, pp. 8433–8442, Nov. 2024.

[25] F. Giusti, Q. Chen, F. Mesa, M. Albani, and O. Quevedo-Teruel, "Efficient bloch analysis of general periodic structures with a linearized multimodal transfer-matrix approach," *IEEE Trans. Antennas Propag.*, vol. 70, no. 7, pp. 5555–5562, Jul. 2022.

[26] M. Ebrahimpouri, A. Algaba Brazalez, L. Manholm, and O. Quevedo-Teruel, "Using glide-symmetric holes to reduce leakage between waveguide flanges," *IEEE Microw. Wireless Compon. Lett.*, vol. 28, no. 6, pp. 473–475, Jun. 2018.

[27] S. Yang, F. Mesa, O. Zetterstrom, S. Clendinning, and O. Quevedo-Teruel, "Understanding the dispersion diagrams of two-dimensional supercells," in *Proc. Microw. Medit. Symp. (MMS)*, May 2022, pp. 1–4.

[28] R. B. Blackman and J. W. Tukey, "The measurement of power spectra from the point of view of communications engineering—Part I," *Bell Syst. Tech. J.*, vol. 37, no. 1, pp. 185–282, Jan. 1958.

[29] R. C. Rumpf. (2013). *Lecture 6 (CEM)—Periodic Structures*. Accessed: Jan. 30, 2025. [Online]. Available: https://www.youtube.com/watch?v=ZS7sl2qmZ-w

[30] Q. Chen, F. Mesa, X. Yin, and O. Quevedo-Teruel, "Accurate characterization and design guidelines of glide-symmetric holey EBG," *IEEE Trans. Microw. Theory Techn.*, vol. 68, no. 12, pp. 4984–4994, Dec. 2020.

[31] M. Petek, J. A. T. Vasquez, G. Valerio, F. Mesa, O. Quevedo-Teruel, and F. Vipiana, "Numerical validation of the multi-modal transfer matrix method for hexagonal unit cells," in *Proc. IEEE Int. Symp. Antennas Propag. INC/USNC-URSI Radio Sci. Meeting (AP-S/INC-USNC-URSI)*, Jul. 2024, pp. 617–618.

[32] N. Castro, M. Saavedra-Melo, E. Rajo-Iglesias, and F. Capolino, "Wide band interaction impedance and mode excitation in glide symmetric double corrugated waveguides for mm-Wave TWTs," *IEEE Trans. Electron Devices*, vol. 70, no. 10, pp. 5400–5407, Oct. 2023.

[33] F. Ghasemifard, M. Norgren, and O. Quevedo-Teruel, "Twist and polar glide symmetries: An additional degree of freedom to control the propagation characteristics of periodic structures," *Sci. Rep.*, vol. 8, no. 1, p. 11266, Jul. 2018.

[34] P. Padilla, L. F. Herrán, A. Tamayo-Domínguez, J. F. Valenzuela-Valdés, and O. Quevedo-Teruel, "Glide symmetry to prevent the lowest stopband of printed corrugated transmission lines," *IEEE Microw. Wireless Compon. Lett.*, vol. 28, no. 9, pp. 750–752, Sep. 2018.

[35] N. J. Higham, D. S. Mackey, and F. Tisseur, "The conditioning of linearizations of matrix polynomials," *SIAM J. Matrix Anal. Appl.*, vol. 28, no. 4, pp. 1005–1028, Jan. 2006, doi: 10.1137/050628283.


**Martin Petek** (Member, IEEE) received the B.Sc. degree in electrical engineering from the University of Ljubljana, Ljubljana, Slovenia, in 2017, the M.Sc. degree in electrophysics from the KTH Royal Institute of Technology, Stockholm, Sweden, in 2020, and the Ph.D. degree (cum laude) from the Politecnico di Torino, Turin, Italy, in 2025.

He is currently with the Department of Electronics and Telecommunications, Politecnico di Torino, as a Post-Doctoral Researcher. His current research interests include numerical techniques, periodic structures, and higher symmetries.

**Jorge Alberto Tobón Vásquez** (Member, IEEE) received the bachelor's degree in electronics engineering from the Universidad de Antioquia, Medellín, Colombia, in 2010, and the master's and Ph.D. degrees in electronics and telecommunication from the Politecnico di Torino, Turin, Italy, in 2010 and 2014, respectively.

Since 2024, he has been with Wavision srl (Politecnico di Torino spin-off), Turin. His main research activities correspond to modeling, designing, and analyzing systems for microwave imaging applications, and the numerical modeling of complex and nonhomogeneous media propagation.

Dr. Vásquez received the "Premio Latmiral," an award granted by the Italian Society of Electromagnetism (SIEM) in 2018, the URSI General Assembly Scientific Symposium (GASS) Young Scientist Award (YSA) in 2020, and the Sorrentino URSI Italy National Meeting Young Scientist Paper Award.

**Guido Valerio** (Senior Member, IEEE) received the M.S. degree (cum laude and Hons.) in electronic engineering and the Ph.D. degree in electromagnetics from La Sapienza University, Rome, Italy, in 2005 and 2009, respectively.

From February to August 2008, he was a Visiting Scholar with the University of Houston, Houston, TX, USA. From 2011 to 2014, he was a Researcher with the Institute d'Electronique et de Télécommunications de Rennes (IETR), Rennes, France. Since September 2014, he has been with the Sorbonne Université, Paris, France, where he is currently a Professor with the Laboratoire de Génie Électrique et Électronique de Paris. He was a co-author of the Best Papers in Electromagnetic and Antenna Theory at the European Conference on Antennas and Propagation in 2018 and 2020, and the Best Student Paper Award at the 16th European Conference on Antennas and Propagation in 2022. His scientific research interests involve antenna design and numerical methods for wave propagation and scattering in complex structures, namely, periodic Green's function computation, modal properties of multilayered structures, modeling and design of periodic structures, metamaterials, and substrate-integrated waveguides.

Dr. Valerio was a recipient of the "Leopold B. Felsen Award for Excellence in Electrodynamics" in 2008; the "Barzilai Prize" for the Best Paper at the National Italian Congress of Electromagnetism (XVIII RiNEm) in 2010; and the RMTG Award for Junior Researchers at the IEEE Antennas and Propagation Society Symposium, Memphis, TN, USA, in 2014. He is serving as an Associate Editor for IEEE TRANSACTION ON ANTENNAS AND PROPAGATION and IEEE ACCESS journals. He was the Main Chair of the COST Action SyMat on "Future Communications With Higher Symmetric Engineered Artificial Materials" from 2019 to 2024 and is currently the co-ordinator of the MSCA Doctoral Network GENIUS "Glide-symmetric metamaterials for innovative radio frequency communication and sensing."

**Francisco Mesa** (Fellow, IEEE) received the Licenciado and Ph.D. degrees in physics from the Universidad de Seville, Seville, Spain, in 1989 and 1991, respectively.

He is currently a Professor with the Departamento de Física Aplicada 1, Universidad de Seville. His research interests include electromagnetic propagation/radiation in microwave and quasioptical structures.

Dr. Mesa is currently a Topic Editor of IEEE JOURNAL OF MICROWAVES.

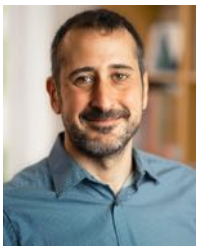

**Oscar Quevedo-Teruel** (Fellow, IEEE) received the Telecommunication Engineering and Ph.D. degrees from Carlos III University of Madrid, Madrid, Spain, in 2005 and 2010, respectively.

From 2010 to 2011, he joined the Department of Theoretical Physics of Condensed Matter, Universidad Autonoma de Madrid, as a Research Fellow, and went on to continue his Post-Doctoral Research with Queen Mary University of London, London, U.K., from 2011 to 2013. In 2014, he joined KTH Royal Institute of Technology, Stockholm, Sweden, where he is a Professor with the Division of Electromagnetic Engineering and Fusion Science and Director of the Master Program in Electromagnetics Fusion and Space Engineering. He has co-authored more than 150 articles in international journals and 250 articles at international conferences. He has made scientific contributions to higher symmetries, transformation optics, lens antennas, and periodic structures.

Dr. Quevedo-Teruel has been a member of European Association on Antennas and Propagation (EurAAP) Board of Directors since January 2021. Since January 2022, he has been the Vice-Chair of EurAAP. He was a Distinguished Lecturer of IEEE Antennas and Propagation Society from 2019 to 2021. He has been an Associate Editor of IEEE TRANSACTIONS ON ANTENNAS AND PROPAGATION from 2018 to 2022 and a Track Editor since 2022.

**Francesca Vipiana** (Senior Member, IEEE) received the Laurea and Ph.D. degrees in electronic engineering from the Politecnico di Torino, Turin, Italy, in 2000 and 2004, respectively.

From 2005 to 2008, she was a Research Fellow with the Department of Electronics, Politecnico di Torino. From 2009 to 2012, she was the Head of the Antenna and EMC Laboratory, Istituto Superiore Mario Boella, Turin. Since 2012, she has been an Assistant Professor with the Department of Electronics and Telecommunications, Politecnico di Torino, where she has been an Associate Professor, since 2014, and a Full Professor, since 2021. Her doctoral research was carried out partly at the European Space Research Technology Center, Noordwijk, The Netherlands. Her main research activities concern numerical techniques based on integral equations and the method of moments, with a focus on multiresolution and hierarchical schemes, domain decomposition, preconditioning, and fast solution methods, and advanced quadrature integration schemes, and she is involved in the numerical modeling and analysis of glide-periodic structures. Moreover, her research interests include the modeling, design, realization, and testing of microwave imaging and sensing systems for medical and industrial applications.

Dr. Vipiana is a member of the EurAAP Board of Directors. She received the Lot Shafai Mid-Career Distinguished Award from the IEEE Antennas and Propagation Society (AP-S) in 2017. She is the Vice-Chair of the IEEE AP-S Expanding Collaboration and Engagement (ECE) Committee. She was an Associate Editor of IEEE TRANSACTIONS ON ANTENNAS AND PROPAGATION from 2018 to 2024 and the Founder and Responsible of the Women in Engineering Column in *IEEE Antennas and Propagation Magazine* from 2019 to 2024.

Open Access funding provided by 'Politecnico di Torino' within the CRUI CARE Agreement